PERGAMON

International Journal of Heat and Mass Transfer 44 (2001) 1869–1888

International Journal of HEAT and MASS TRANSFER

www.elsevier.com/locate/ijhmt

Axial interfacial area transport of vertical bubbly flows

Takashi Hibiki [a], Mamoru Ishii [b,*], Zheng Xiao [b]

[a] *Department of Nuclear Energy Science, Research Reactor Institute, Kyoto University, Kumatori-cho, Sennan-gun, Osaka 590-0494, Japan*

[b] *School of Nuclear Engineering, Purdue University, West Lafayette, IN 47907-1290, USA*

Received 14 January 2000; accepted 11 July 2000

Abstract

Recently, the concept of the interfacial area transport equation has been proposed to develop the constitutive relation on the interfacial area concentration in relation to the modeling of the interfacial transfer terms in the two-fluid model. Accurate data sets on axial development of local flow parameters such as void fraction, interfacial area concentration, interfacial and liquid velocities and turbulence intensity are indispensable to verify the modeled source and sink terms in the interfacial area transport equation. From this point of view, local flow measurements of vertical upward air–water flows in a round tube with an inner diameter of 50.8 mm were performed at three axial locations of $z/D = 6.00$, 30.3 and 53.5 as well as 15 radial locations from $r/R = 0$–0.95 by using the double-sensor probe and the hotfilm probe. In the experiment, the superficial liquid velocity and the void fraction ranged from 0.491 to 5.00 m/s and from 4.90% to 44.2%, respectively. The flow condition covered extensive region of bubbly flows including finely dispersed bubbly flow as well as bubbly-to-slug transition flow. The combined data from the double-sensor probe and the hotfilm probe give near complete information on the time averaged local hydrodynamic parameters of two-phase flow. This data can be used for the development of reliable constitutive relations which reflect the true transfer mechanisms in two-phase flow.

Keywords: Interfacial area transport; Two-fluid model; Void fraction; Interfacial area concentration; Bubble size; Turbulence; Resistivity probe; Hotfilm anemometry; Gas–liquid bubbly flow; Multiphase flow

1. Introduction

In the past 25 years, significant developments in the two-phase flow formulation have been accomplished by the introduction of the drift flux model and the two-fluid model. In the present state-of-the-art, the two-fluid model is the most detailed and accurate macroscopic formulation of the thermo-fluid dynamics of two-phase systems. In the two-fluid model, the field equations are expressed by the six conservation equations consisting of mass, momentum and energy equations for each phase. Since these field equations are obtained from an appropriate averaging of local instantaneous balance equations, the phasic interaction term appears in each of the averaged balance equations. These terms represent the mass, momentum and energy transfers through the interface between the phases. The existence of the interfacial transfer terms is one of the most important characteristics of the two-fluid model formulation. These terms determine the rate of phase changes and the degree of mechanical and thermal non-equilibrium between phases, thus they are the essential closure relations which should be modeled accurately. However, because of considerable difficulties in terms of measurements and modeling, reliable and accurate closure relations for the interfacial transfer terms are not fully developed.

A detailed mathematical analysis as well as physical insight indicate that the interfacial transfer terms are proportional to the interfacial area concentration and driving force for that particular transfer [1]. The interfacial area concentration is the available interfacial area per unit volume of a mixture, and, therefore represents the geometrical effects of the interfacial structure,

* Corresponding author. Tel.: +1-765-494-4587; fax: +1-765-494-9570.

E-mail address: ishii@ecn.purdue.edu (M. Ishii).

0017-9310/01/$ - see front matter
PII: S0017-9310(00)00232-5

Nomenclature

a_i	interfacial area concentration
D	pipe diameter
D_B	bubble diameter
D_{Sm}	Sauter mean diameter
Eo	Eötvös number ($\equiv g\Delta\rho D_B{}^2/\sigma$)
f	sampling frequency
g	gravitational acceleration
$I(\omega_0)$	correction factor
j_g	superficial gas velocity
j_f	superficial liquid velocity
L	pipe length
N_t	number of bubbles which pass the point per unit time
P	pressure
R	tube radius
Re	Reynolds number ($\equiv\rho jD/\mu$)
r	radial coordinate
S_j	source or sink terms in the interfacial area concentration due to bubble breakup or coalescence, respectively
S_{ph}	source or sink term in the interfacial area concentration due to phase change
t	time
V_{gj}	drift velocity
v_g	interfacial velocity
$\overrightarrow{v_g}$	average local interfacial velocity weighted by the bubble number
v_f	liquid velocity
v_f'	liquid turbulence fluctuation
v_{sz}	passing velocity of jth interface through the double sensor probe in mean flow direction
z	z-coordinate

Greek symbols

α	void fraction
β	volumetric flow rate quality defined by $\langle j_{g,0}\rangle/(\langle j_{g,0}\rangle + \langle j_f\rangle)$
$\Delta\rho$	density difference
μ	viscocity
δ_B	distinguishable liquid-layer thickness between bubbles by double sensor probe
ξ	interfacial area change due to bubble coalescence or breakup
σ	interfacial tension
σ_z	root mean square of fluctuations of z-component interfacial velocity
τ	minimum response time of the circuit
ψ	factor depending on the shape of a bubble ($1/36\pi$ for a spherical bubble)
ω_0	maximum angle between velocity vector of jth interface and mean flow direction vector

Subscripts

0	inlet
B	small bubble
C	cap bubble
eq	equilibrium state
HF	measured by hotfilm anemometer
max	maximum value
MGM	measured by a magnetic flow meter
Probe	measured by a double sensor probe

Mathematical symbols

$\langle\rangle$	area averaged quantity
$\langle\langle\rangle\rangle$	void fraction weighted cross-sectional area averaged quantity
$\langle\langle\rangle\rangle_a$	interfacial area concentration weighted cross-sectional area averaged quantity
$-t$	time average

whereas the driving force represents the physical force which induces that transfer. The interfacial area concentration is unique to two-phase flow and require special attention. In view of its great importance to two-fluid model, the interfacial area concentration has been studied intensively in the past 10 years. Recently, the introduction of the interfacial area transport equation has been recommended to improve the two-fluid model [2,3]. It can replace the traditional flow regime maps and regime transition criteria. The changes in the two-phase flow structure are predicted mechanistically by introducing the interfacial area transport equation. The effects of the boundary conditions and flow development are efficiently modeled by this transport equation. Thus a successful development of the interfacial area transport equation can make a quantum improvement in the two-fluid model formulation. A research strategy to accomplish the development of the interfacial area transport equation would be classified into the following sub-divided five projects, namely: (1) the formulation of the interfacial area transport equation, (2) the development of measurement techniques for local flow parameters, (3) the construction of a data base, (4) the modeling of sink and source terms in the interfacial area transport equation, and (5) the improvement of thermal hydraulic system analysis code by introducing the interfacial area transport equation.

As for (1), Kocamustafaogullari and Ishii [4] formulated a one-dimensional transport equation for predicting the average bubble number density by considering a boiling channel with a constant cross-sectional area. Reyes [5] developed a particle number density transport equation for chemically non-reacting, dispersed spherical fluid particles from a population balance approach. For the purpose to take account of interfacial area transport, Kocamustafaogullari and

Ishii [6] generalized Reyes's model, then taking a moment of number density with interfacial area, they obtained the interfacial area transport equation based on statistical mechanics. Recently, Ishii et al. [7] proposed the general approach to treat the bubbles in two groups: the spherical/distorted bubble group and the cap/slug bubble group, resulting in two bubble number density transport equations that involve the inner and inter group interactions. Morel et al. [8] also derived local volumetric interfacial area transport equation from geometrical considerations. As for (2), a theoretical study carried out at Argonne National Laboratory by Kataoka and Ishii [9] showed that the local time averaged interfacial area concentration could be uniquely related to the harmonic mean of the interfacial velocity. This opened up a way to measure the interfacial area directly through the velocity measurement. Using the theoretically supported method, double-sensor and multi-sensor probes were developed to measure local void fraction, interfacial area concentration, and interfacial velocity [10–13]. Kalkach-Navarro [14] also conducted local measurements by the double-sensor probe with a theoretical model derived from the assumptions that the bubbles were spherical and that their size could be represented by a bubble size probability distribution function [15]. Such methods have been improved continuously [16–20]. On the other hand, hotfilm anemometry has been applied to measure local liquid velocity and turbulence intensity [17,21–24]. As for (3), continuous efforts have been made to construct rigorous data base [17,25–32]. As for (4), the preliminary modeling of sink and source terms was performed for the development of the one-group interfacial area transport equation [33,34] and two-group interfacial area transport equations [35]. As for (5), a new method was tested for describing interfacial transport processes based on the explicit modeling of interfacial area concentration and its evolution in time and space [36].

In the present state of the art, scarce rigorous data base would be the weakest point in the development of the interfacial area transport equation. From this point of view, the authors already measured axial development of local flow parameters such as void fraction, interfacial area concentration, interfacial and liquid velocities and turbulence intensity for vertical upward air–water flows in round tubes with inner diameters of 25.4 and 50.8 mm. In the experiment using the 25.4 mm-diameter tube, the superficial liquid velocity and the void fraction ranged from 0.292 to 3.49 m/s and from 1.83% to 26.8%, respectively [32]. In the experiment using the 50.8 mm-diameter tube, the measurement was performed for relatively low superficial liquid velocity (0.600 m/s $\sim$1.30 m/s) and void fraction (2.17–8.43%) [17]. In relation to the construction of the data base, this study focuses on local measurements of vertical upward air–water flows in a round tube with an inner diameter of 50.8 mm over an extensive flow condition. The measurements were performed at three axial locations of $z/D = 6.00$, 30.3 and 53.5 as well as fifteen radial locations from $r/R = 0$–0.95 by using the double-sensor probe and the hotfilm probe. In the present experiment, the superficial liquid velocity and the void fraction ranged from 0.491 to 5.00 m/s and from 4.90% to 44.2%, respectively. The flow condition covered extensive region of bubbly flows including finely dispersed bubbly flow as well as bubbly-to-slug transition flow. The combined data from the double-sensor probe and the hotfilm probe give near complete information on the time averaged local hydrodynamic parameters of two-phase flow. This data can be used for the development of reliable constitutive relations which reflect the true transfer mechanisms in two-phase flow.

2. Experimental

2.1. Double sensor probe methodology

Local flow parameters such as void fraction, interfacial area concentration, interfacial velocity and bubble diameter were measured by a double sensor probe. The double sensor probe was used basically as a phase identifier of the two-phase mixture. The double sensor probe consisted of two sensors made of platinum–rhodium (13% Rh) wire with a diameter of 0.127 mm. The two wires were adjusted for typical distance of approximately 2–3 mm in the length wise direction and were aligned in the axial direction. The information to be recorded from each signal were the number of bubbles that had hit the sensor, the time that the sensor was exposed to the gas phase, and the relative time between the bubble hitting the upstream and downstream sensor. The time-averaged interfacial velocity, v_g, was calculated by taking into account the distance between the tips of the upstream and downstream sensor and the time difference between the upstream and downstream signal. The time-averaged void fraction, α, was simply the accumulated time the sensor was exposed to the gas phase divided by the total sampling time of the sensor. It has been shown mathematically that the interfacial area concentration, a_i, equals the harmonic mean of the interfacial velocity. The theoretical base of this measurement technique was given by Kataoka and Ishii [9]. Recently, the basic equation has been improved by Hibiki and Ishii [17]. The following equation can be derived based on the assumptions that: (i) the number of measured interfaces is large, (ii) interfacial velocity is statistically independent of the angle between mean flow direction (z-direction) and normal direction of jth interface, (iii) the interfaces are composed of spherical bubbles, (iv) the probe passes every part of a bubble with an equal probability and (v) transverse

direction (x- or y-direction) components of interfacial velocity are random [17].

$$a_i = 2N_t \frac{\overline{1}^t}{\left|\overrightarrow{v_{sz}}\right|} I(\omega_0), \quad I(\omega_0) = \frac{\omega_0^3}{3(\omega_0^3 - \sin\omega_0)}, \tag{1}$$

where N_t, v_{sz}, and ω_0 denote the number of bubbles which pass the point per unit time, the passing velocity of the jth interface through the double sensor probe in the z-direction, and the maximum angle between the velocity vector of the jth interface and z-direction vector, respectively. The relationship between the maximum angle and the interfacial velocity can be derived based on the assumption that the root mean square of the fluctuations of the z-component interfacial velocity, σ_z, is equal to that of the root mean square of the x- and y-component velocity fluctuations.

$$\frac{3}{2\omega_0^2}\left(1 - \frac{\sin 2\omega_0}{2\omega_0}\right) = \frac{1 - (\sigma_z^2/\overline{\vec{v}_{sz}}^{t^2})}{1 + 3(\sigma_z^2/\overline{|\vec{v}_{sz}|}^{t^2})}, \tag{2}$$

The maximum angle, ω_0, can be calculated by Eq. (2) with measured σ_z and $\overline{\vec{v}_{sz}}^t$. The interfacial area concentration can be calculated from the number of bubbles which pass the point per unit time, and the interfacial velocity with Eqs. (1) and (2). The Sauter mean diameter, D_{Sm}, can be expressed as a function of the time-averaged interfacial area concentration and void fraction, namely $D_{Sm} = 6\alpha/a_i$.

In the strict sense, the assumption of spherical bubbles may not be valid for any bubbly flow systems. Bubble shapes in the present experiment may be ellipsoidal with wobbling interfaces. However, it is considered that the assumption of spherical bubbles would practically work for the interfacial area concentration measurement on the following grounds. The area averaged interfacial area concentrations measured by the double sensor probe method were compared with those measured by a photographic method in relatively low void fraction ($\langle\alpha\rangle \leqslant 8\%$) and wide superficial liquid velocity (0.262 m/s $\leqslant \langle j_f\rangle \leqslant$ 3.49 m/s) conditions where the photographic method could be applied [17]. As shown in a figure at the upper right of Fig. 1, good agreement was obtained between them within the relative deviation of 6.95%. In addition to this, when a spherical bubble is transformed into an ellipsoidal bubble with the aspect ratio of 2, the resulting increase of the interfacial area is estimated mathematically to be less than 10% [37].

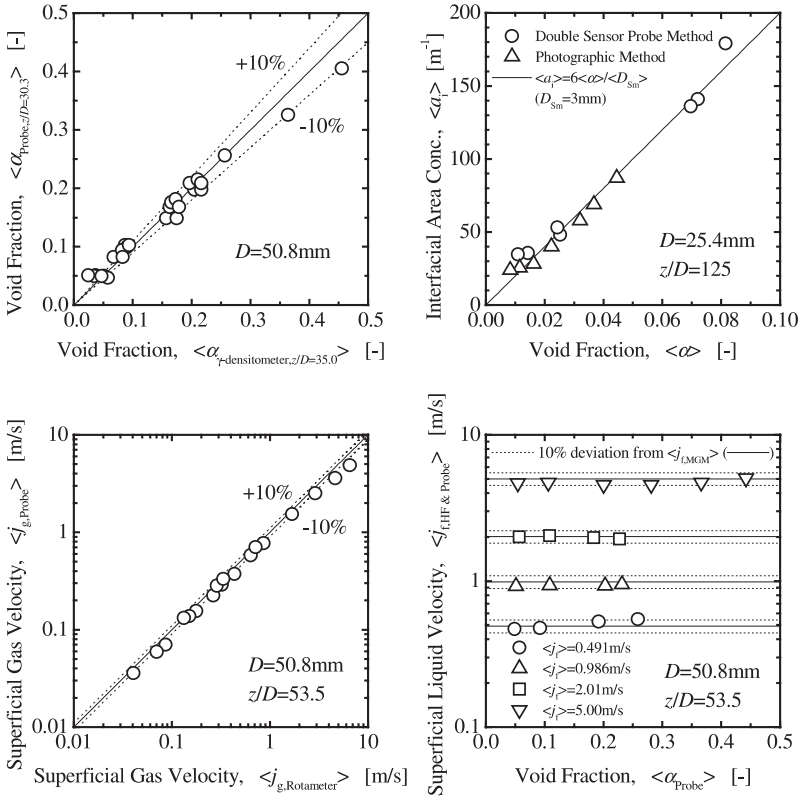

Fig. 1. Verification of the double sensor probe and hot film probe methods with other calibration methods.

As for the assumption of isotropic turbulence, the study carried out by Hilgert and Hofmann [38] for bubbly flow in a vertical pipe using the ultrasonic Doppler technique has shown that the magnitude of the axial component of the root mean squares of bubble velocity fluctuation was nearly equal to the transverse components of the root mean squares of the fluctuations of bubble velocity at low superficial gas velocities. Several researches on the interfacial area measurement have been performed by the double sensor probe method based on the assumption of spherical bubbles [9–12,14,16,17,19,25,27–32]. However, it is considered that future studies should focus on rigorous formulation of the interfacial area concentration taking account of the bubble shape with deformed interface, and measurement of local liquid turbulence over wide range of flow conditions.

Using a fast A/D converter Metrabyte DAS-20 board and an IBM/PC-XT computer, local flow measurements were conducted in a data acquisition program. The acquisition board has a maximum sampling rate of 100 000 cycles per second. For the data sets measured with the double sensor probe, a minimum of 2000 bubbles were sampled to maintain similar statistics between the different combinations of gas flow rates. Here, in the void fraction measurement at bubbly-to-slug flow transition, bubbles were separated into either a cap bubble or a small bubble based on the double-sensor probe signals [30,32]. The determination whether detected bubbles were cap bubbles was performed based upon the chord length of bubbles. According to Clift's shape regime map for bubbles [39], the boundary between ellipsoidal and spherical-cap bubbles is given by $Eo\ (\equiv g\Delta\rho D_B^2/\sigma) = 40$, which corresponds to the bubble diameter of 17.2 mm in an air–water system at 20°C. In the present experiment, when local bubble chord length exceeded 20 mm, bubbles were considered as cap bubbles. Thus, the void fraction for each category was obtained by the double sensor probe separately. It should be noted here that the signals for cap bubbles were not acquired in the measurement of the interfacial area concentration as well as the Sauter mean diameter but the void fraction. The Sauter mean diameter in the high void fraction region where cap bubbles appeared was calculated from $D_{Sm} = 6\alpha/a_i \approx 6\alpha/(a_i - a_{i,C})$, since the contribution of cap bubbles to total interfacial area concentration would be relatively small (see Appendix A); for example, $a_{i,C}/a_i = 3.45\%$ for $\alpha_C/\alpha = 0.5$ and $D_C/D_B = 10$ [32]. Therefore, it is expected that even data taken at the bubbly-to-slug transition flow would be used for evaluation of modeled sink and source terms in one-group interfacial area transport equation as well as two-group interfacial area transport equations [32].

In the measurement using the double sensor probe, the distinguishable liquid-layer thickness between bubbles, δ_B, may be roughly estimated by the interfacial velocity, v_g, the sampling frequency, f, and the minimum response time of the circuit, τ, that is $\delta_B \approx \max[v_g/f, v_g \cdot \tau]$. In the present data acquisition system, the distinguishable liquid-layer thickness between bubbles is roughly estimated to be 0.3 mm. Therefore, the double sensor probe may not distinguish each bubble in a large bubble cluster consisted of a cap bubble and small bubbles at the bubbly-to-slug flow transition boundary, when they are tightly packed. The double sensor probe methodology was detailed in the previous paper [12,17,32,37].

It should be noted here that the double sensor probe method may not work in the vicinity of a wall. The presence of the wall does not allow a bubble to pass the probe randomly as in the other positions in the pipe. This fact will cause a measurement error in the interfacial area concentration, interfacial velocity and Sauter mean diameter. The range where the double sensor probe method can work may be roughly estimated as $0 \leqslant r/R \leqslant 1 - D_B/D$. In this experiment ($D = 50.8$ mm), the effective range of the double sensor probe is $0 \leqslant r/R \leqslant 0.92$ or $0 \leqslant r/R \leqslant 0.96$ for $D_B = 4$ or 2 mm, respectively. The detailed discussion was given by Kalkach-Navarro et al. [14].

2.2. Hotfilm anemometer methodology

Local flow parameters such as liquid velocity, v_f, and liquid velocity fluctuation, v_f', in a two-phase flow were measured by using a hotfilm anemometer system FLOWPOINT, which TSI Incorporated developed for liquid velocity and turbulence intensity measurements in a single-phase flow. The FLOWPOINT system is a fully-integrated, thermal anemometer-based system that measures the local fluid velocity and local fluid temperature. The probe used in this experiment was the TSI Model 1264 AW designed with a conical tip. The tip had a sensor diameter of 1.27 mm and a sensor length of 1 mm. The hotfilm probe was calibrated with an electromagnetic flow meter. In order to obtain the liquid velocity representative of the flow, it was necessary to filter out the voltage depressions and spikes due to the bubbles hitting and passing the probe. The voltage spikes were removed from the signal using threshold and maximum slope schemes [17,24,40]. After the bubbles were removed from the signal, the voltages from the hotfilm probe was converted to velocities using the calibration curve and the statistical parameters identifying the turbulent flow was calculated. In this experiment, a sampling rate was set at either 5000 or 10 000 cycles per second in accordance with a liquid velocity. In this study, the turbulence intensity was defined by $v_f'/v_{f,max}$. The hotfilm anemometer methodology was detailed in the previous paper [17,32,40].

2.3. Two-phase flow experiment

The two-phase flow experiment was performed by using a flow loop installed at Thermal-Hydraulics and Reactor Safety Laboratory in Purdue University. Fig. 2 shows the schematic diagram of a two-phase flow loop. The test section was a round tube made of an acrylic resin. Its inner diameter and length were 50.8 and 3061 mm, respectively, and L/D of the test section was 60.3. Air was supplied by a compressor and was introduced into a mixing chamber through a porous media with the pore size of 40 μm. The air and purified water were mixed in the mixing chamber and the mixture flowed upwards through the test section. After flowing through the test section, the air was released into the atmosphere through a separator, while the water was circulated by a centrifugal pump. The flow rates of the air and water were measured with a rotameter and a magnetic flow meter, respectively. The loop temperature was kept at a constant temperature (20°C) within the deviation of ±0.2°C by a heat exchanger installed in a water reservoir. The local flow measurements using the double sensor and hotfilm probes were performed at three axial locations of $z/D = 6.00$, 30.3, and 53.5 and 15 radial locations from $r/R = 0$ to 0.95. A γ-densitometer was installed at $z/D = 35.0$ in the loop to measure the area averaged void fraction. The pressure measurements were also conducted by Bourdon-tube pressure gauges at above three measuring stations. The area averaged superficial liquid velocities, $\langle j_f \rangle$, and the area averaged superficial gas velocities at the inlet, $\langle j_{g,0} \rangle$, in this experiment are tabulated in Table 1. The flow conditions covered most of a bubbly flow region, including finely dispersed bubbly flow and bubbly-to-slug transition flow regions. The area averaged superficial gas velocities were roughly determined so as to provide the same area averaged void fractions among different conditions of superficial liquid velocity, namely $\langle \alpha_{z/D=53.5} \rangle = 5, 10, 20,$ and 25%. For $\langle j_f \rangle = 5.00$ m/s, additional experiments were performed for flow conditions with void fractions of 35% and 44%, corresponding to the finely-dispersed bubbly flow condition. It should be noted here that void fraction increased along the axial direction on the order of 20–40% between $z/D = 6.00$ and 53.5 in the present experimental conditions due to the pressure reduction. This led to a continuous developing flow along the flow direction.

Generally, a void distribution depends on an initial condition (bubble size, generation method and mixing condition), a flow condition (flow rates and physical properties), and a test section condition (geometry and wall surface) [10,25,41]. Among them, the conditions except for the initial condition was the same in this experiment. Although sophisticated experiments controlling the initial condition were performed [10,25,41], the initial condition was not controlled in this experiment, resulting in the change of the initial bubble size with the flow condition. Fig. 3 shows the dependence of the initial bubble size measured at $z/D = 6.00$ on the inlet void fraction obtained from the extrapolation of the axial change in the void fraction, or the superficial liquid velocity. The initial bubble size increased with increasing the gas flow rate, whereas it decreased with increasing the liquid flow rate. The increase in the gas

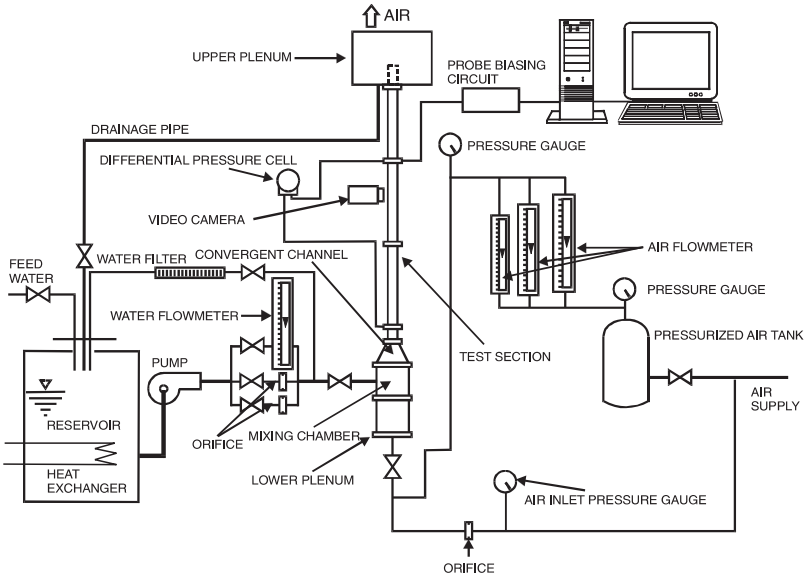

Fig. 2. Schematic diagram of experimental loop.

Table 1
Flow conditions in this experiment[a]

Symbols $\langle j_f \rangle$ (m/s)	● $\langle j_{g,0} \rangle$ (m/s)	▲ $\langle j_{g,0} \rangle$ (m/s)	■ $\langle j_{g,0} \rangle$ (m/s)	▼ $\langle j_{g,0} \rangle$ (m/s)	◆ $\langle j_{g,0} \rangle$ (m/s)	* $\langle j_{g,0} \rangle$ (m/s)
0.491	**0.0275**	**0.0556**	**0.129**	**0.190**	N/A	N/A
$Re_f = 2.48 \times 10^4$						
$(\langle \alpha_{z/D=53.5} \rangle$ [%])	(4.90)	(9.20)	(19.2)	(25.9)		
$(Re_{g,0})$	(89.6)	(181)	(420)	(619)		
0.986	**0.0473**	**0.113**	**0.242**	**0.321**[b]	N/A	N/A
$Re_f = 4.99 \times 10^4$						
$(\langle \alpha_{z/D=53.5} \rangle$ [%])	(5.12)	(10.8)	(20.3)	(23.1)		
$(Re_{g,0})$	(154)	(368)	(788)	(1050)		
2.01	**0.103**	**0.226**	**0.471**[b]	**0.624**[b]	N/A	N/A
$Re_f = 1.02 \times 10^5$						
$(\langle \alpha_{z/D=53.5} \rangle$ [%])	(5.68)	(10.8)	(18.3)	(22.8)		
$(Re_{g,0})$	(335)	(736)	(1530)	(2030)		
5.00	**0.245**	**0.518**	**1.11**[b]	**1.79**[b]	**2.87**[b]	**3.90**[b]
$Re_f = 2.53 \times 10^5$						
$(\langle \alpha_{z/D=53.5} \rangle$ [%])	(5.41)	(10.6)	(20.0)	(28.1)	(36.6)	(44.2)
$(Re_{g,0})$	(798)	(1690)	(3610)	(5830)	(9350)	(12 700)

[a] Values in the parentheses mean the void fractions in % measured at $z/D = 53.5$. Valued in the double parentheses mean the Reynolds number of gas phase at the inlet.
[b] Cap bubbles were observed in these flow conditions.
N/A = not available.

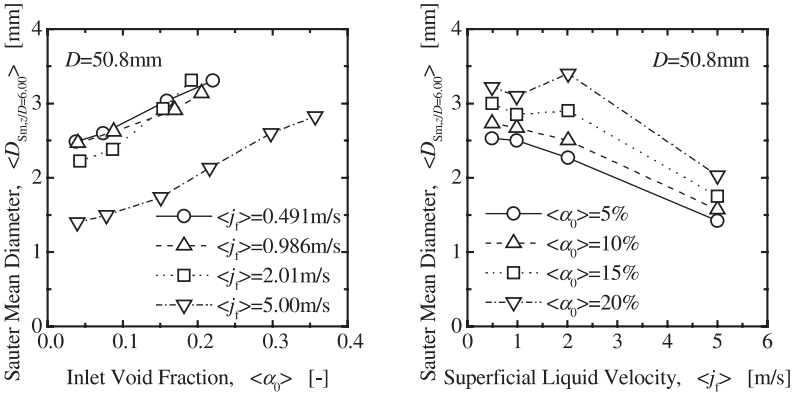

Fig. 3. Dependence of initial bubble size on superficial gas and liquid velocities.

flow rate would enhance the bubble coalescence due to the collision of bubbles, resulting in the increase of the initial bubble size. On the other hand, the increase in the liquid flow rate would enhance the bubble breakup due to the liquid turbulence, resulting in the decrease of the initial bubble size. However, the effect of the liquid flow rate on the initial bubble size was not pronounced for $\langle j_f \rangle \leqslant 2$ m/s, where the liquid turbulence might not be large enough to disintegrate the bubbles. In this experiment, bubbles with the size of about 3 and 2 mm were generated at the inlet for $\langle j_f \rangle \leqslant 2$ m/s and $\langle j_f \rangle = 5$ m/s, respectively.

In order to verify the accuracy of local measurements, the area averaged quantities obtained by integrating the local flow parameters over the flow channel were compared with those measured by other cross-calibration methods such as the γ-densitometer for void fraction, the photographic method for interfacial area concentration, the rotameter for superficial gas velocity, and the magnetic flow meter for superficial liquid velocity.

Area averaged superficial gas velocity was obtained from local void fraction and gas velocity measured by the double sensor probe, whereas area averaged superficial liquid velocity was obtained from local void fraction measured by the double sensor probe and local liquid velocity measured by hotfilm anemometry. As shown in Fig. 1, good agreements were obtained between the area averaged void fraction, interfacial area concentration, superficial gas velocity and superficial liquid velocity obtained from the local measurements and those measured by the γ-densitometer, the photographic method, the rotameter and the magnetic flow meter within the error of 5.74%, 6.95%, 12.4%, and 5.19%, respectively. It should be noted here that the cross-calibration experiment using the photographic method was performed in an experimental loop consisted of a round tube with an inner diameter of 25.4 mm [12]. The photographic method might not be applicable to a relatively high void fraction region particularly in a larger diameter pipe, since the decrease in the ratio of the bubble diameter to the tube diameter would enhance the possibility of a bubble overlapping.

3. Results and discussion

3.1. Local flow parameters

3.1.1. Void fraction

Fig. 4 shows the behavior of void fraction profiles measured at $z/D = 6.00$ (upper figures) and 53.5 (lower figures) in this experiment. The meanings of the symbols in Fig. 4 are found in Table 1. Serizawa and Kataoka [42] classified the phase distribution pattern into four basic types of distributions, that is, "wall peak" (for example, $\langle j_{g,0}\rangle = 0.0473$ m/s, $\langle j_f\rangle = 0.986$ m/s, $z/D = 53.5$; ●) "intermediate peak" (for example, $\langle j_{g,0}\rangle = 0.226$ m/s, $\langle j_f\rangle = 2.01$ m/s, $z/D = 53.5$; ▲), "core peak" (for example, $\langle j_{g,0}\rangle = 3.90$ m/s, $\langle j_f\rangle = 5.00$ m/s, $z/D = 53.5$; *), and "transition" (for example, $\langle j_{g,0}\rangle = 0.321$ m/s, $\langle j_f\rangle = 0.986$ m/s, $z/D = 53.5$; ▼). In addition to these basic patterns of the phase distribution, "flat " distribution was observed for $\langle j_f\rangle = 5.00$ m/s and $\langle\alpha\rangle < 15\%$ (for example, $\langle j_{g,0}\rangle = 0.245$ m/s, $\langle j_f\rangle = 5.00$ m/s, $z/D = 53.5$; ●). Fig. 5 shows maps of phase distribution patterns observed at $z/D = 6.00$ and 53.5. The open

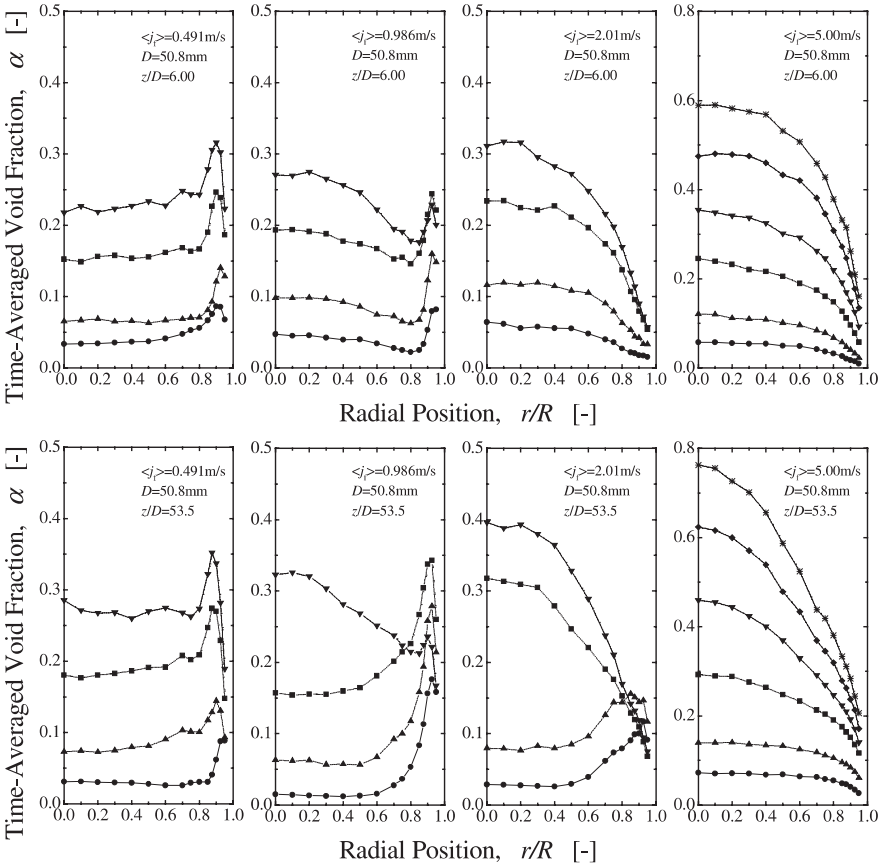

Fig. 4. Local void fraction profiles at $z/D = 6.00$ and 53.5.

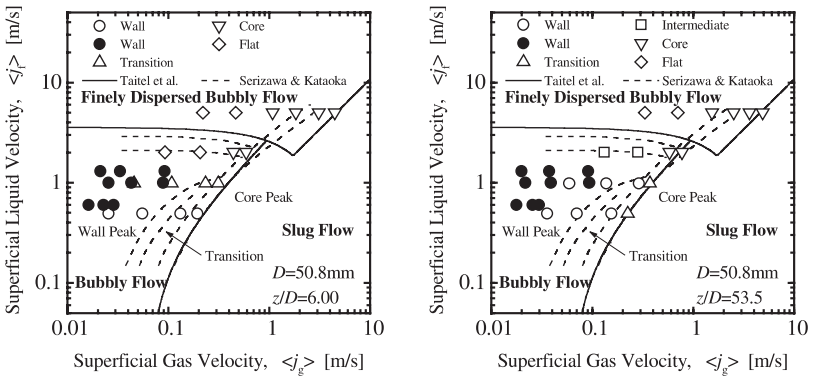

Fig. 5. Maps of phase distribution patterns at $z/D = 6.00$ and 53.5.

symbols of circle, triangle, square, reversed triangle, and diamond in Fig. 5 indicate the wall peak, the transition, the intermediate peak, the core peak, and the flat, respectively, observed in this experiment. The solid symbol of circle means the wall peak observed at $z/D = 2.00$ (left figure in Fig. 5) or 62.0 (right figure in Fig. 5) in the previous experiment with a different bubble generator [17]. The solid and broken lines in Fig. 5 are the flow regime transition boundaries predicted by the model of Taitel et al. [43] and the phase distribution pattern transition boundaries, which were developed by Serizawa and Kataoka [42] based on experiments performed by different researchers with different types of bubble injections in round tubes (20 mm $\leqslant D \leqslant$ 86.4 mm). A fairly good agreement was obtained between the Serizawa–Kataoka's map [42] and phase distribution patterns observed at $z/D = 53.5$ except for $\langle j_f \rangle = 5.00$ m/s and $\langle \alpha \rangle < 15\%$, whereas the Serizawa–Kataoka's map did not agree with the observation at $z/D = 6.00$ well. As will be discussed later, the effect of flow developing and bubble size on the phase distribution should be taken into account to establish the map.

For $\langle j_f \rangle = 0.491$ m/s, a well-developed wall peaking was observed even at the first measuring station of $z/D = 6.00$, where Sauter mean diameter was smaller than 3.6 mm as shown in the lower figure in Fig. 6. Zun [44] reported that distinctive higher bubble concentration at the wall region if the bubble equivalent sphere diameter appeared in the range of 0.8 and 3.6 mm. He also pointed out that intermediate void profiles occurred at bubble sizes either between 0.6 and 0.8 mm or 3.6 and 5.1 mm and that bubbles smaller than 0.6 mm or larger than 5.1 mm tended to concentrate at the channel center. For $\langle j_f \rangle = 0.491$ m/s and $\langle \alpha \rangle < 20\%$ (●, ▲, ■), the bubble coalescence due to the bubble collision driven by liquid turbulence as well as the bubble breakup due to turbulent impact might be unlikely to occur because of a small liquid turbulence and a relatively large distance between bubbles. Therefore, the bubble size, which is a key factor to determine the phase distribution, would mainly be changed by the pressure reduction along the flow direction. Local void fraction was gradually augmented along the flow direction by the gas expansion due to the axial pressure reduction, maintaining the phase distribution. The peaks, which were approximately located at a distance equal to the measured mean equivalent bubble radius (for example, the peak location for 4 mm diameter bubble is $r/R = 0.92$), were then shifted toward the tube center as the flow develops. For $\langle j_f \rangle = 0.491$ m/s and $\langle \alpha \rangle > 20\%$ (▼), the bubble coalescence would be enhanced a little because of a relatively small distance between bubbles. Relatively large bubbles ($\langle D_{Sm} \rangle = 3.63$ mm, see Fig. 6) formed at $z/D = 53.5$ by the bubble coalescence had a tendency to migrate toward the channel center [44], resulting in changing the phase distribution from the wall peak to the transition.

For $\langle j_f \rangle = 0.986$ m/s, a transition distribution was observed at the first measuring station, where Sauter mean diameter was smaller than 3.6 mm (see Fig. 6). The wall peaking was pronounced at the third measuring station of $z/D = 53.5$ for $\langle \alpha \rangle < 20\%$ (●, ▲, ■), where the Sauter mean diameter was still smaller than 3.6 mm. On the other hand, the peaking near the center was enhanced at $z/D = 53.5$ for $\langle \alpha \rangle > 20\%$ (▼), where the Sauter mean diameter was larger than 3.6 mm. As shown in Fig. 7, cap bubbles were formed in this flow condition. The ratios of void fraction for cap bubbles to total void fraction, $\langle \alpha_C \rangle / \langle \alpha \rangle$ were 0.241% and 5.42% at $z/D = 6.00$ and 53.5, respectively. In such a flow condition, liquid turbulence would mainly contribute to promotion of collision between bubbles, resulting in enhanced bubble coalescence, since it might not have enough energy to disintegrate bubbles. Relatively large bubbles might move toward the channel center, resulting in the cap bubble formation around the channel center. The cap bubbles formed around the channel center

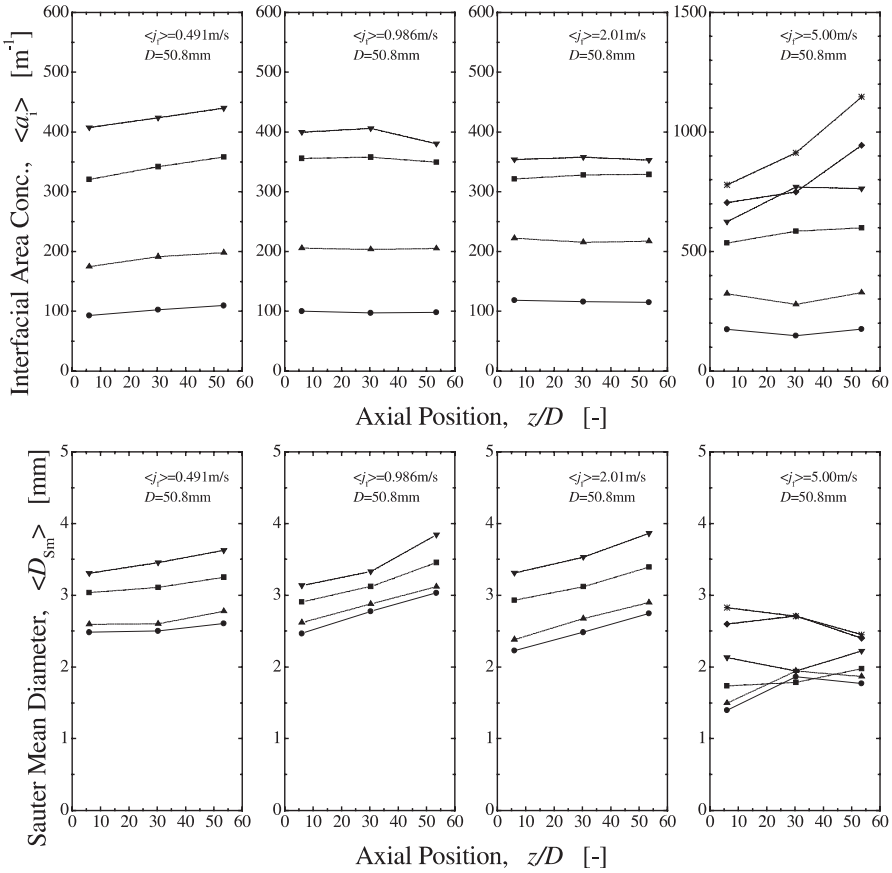

Fig. 6. Axial development of area averaged interfacial area concentration and Sauter mean diameter.

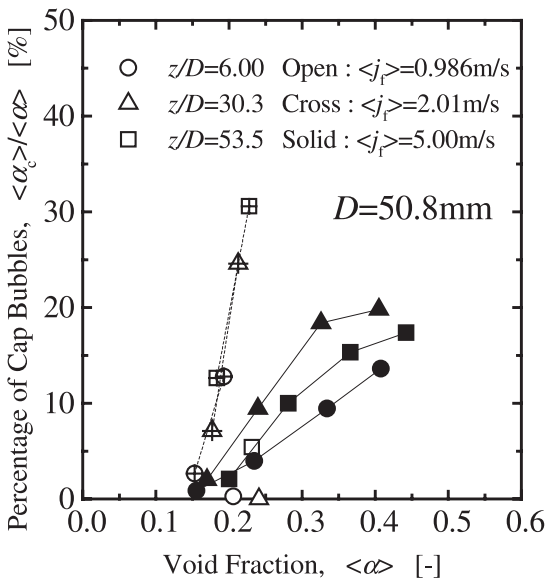

Fig. 7. Percentage of void fraction in a form of cap bubble, $\langle \alpha_C \rangle$.

might not be disintegrated because most of the turbulence kinetic energy was produced and dissipated near the wall. Thus, the cap bubble formation was attributed to enhanced void peak around the channel center.

For $\langle j_f \rangle = 2.01$ m/s, no wall peaking was observed at $z/D = 6.00$, although Sauter mean diameter was smaller than 3.6 mm. However, for $\langle \alpha \rangle < 15\%$, as the flow developed, the small bubbles moved toward the channel wall, resulting in the intermediate void distribution at $z/D = 53.5$. On the other hand, for $\langle \alpha \rangle > 15\%$, cap bubbles were formed as shown in Fig. 7. When bubbles enter the wake region of a leading cap bubble, they will accelerate and may collide with the leading one [45]. As can be seen in Figs. 7 and A1, the void fraction of cap bubbles was gradually increased along the flow direction. Thus, the core peaking was pronounced along the flow direction.

For $\langle j_f \rangle = 5.00$ m/s and $\langle \alpha \rangle < 15\%$, not the intermediate peak suggested by the Serizawa–Kataoka's map but the flat void distribution appeared as shown in Fig. 4. In this flow condition, the void fraction profile was found to be almost flat around the channel center ($r/R < 0.6$). The reason for this phase distribution might

be due to a strong bubble mixing over the flow channel by a turbulence fluctuation. The probability of bubble existence around the channel center might be larger than that near the wall. Local void fraction was gradually augmented along the flow direction by the gas expansion due to the axial pressure reduction, maintaining the phase distribution. For $\langle j_f \rangle = 5.00$ m/s and $\langle \alpha \rangle > 15\%$, a core peak was observed at $z/D = 6.00$. The core peaking was pronounced along the axial direction and a relatively steep peaking near the channel center was observed in the void distribution. In the flow condition, violent bubble coalescence and breakup might be expected to occur due to the strong turbulence fluctuation. Some of large bubbles formed by the coalescence were transported to the channel center, since a large bubble (>3.6 mm) tended to migrate toward the channel center [44]. This led to the enhanced core peaking in the void distribution.

3.1.2. Sauter mean diameter

Fig. 8 shows the behavior of Sauter mean diameter profiles, corresponding to that of void fraction profiles in Fig. 4. Fig. 6 (lower figures) also shows the axial development of one-dimensional Sauter mean diameters, $\langle D_{Sm} \rangle$, obtained by integrating local Sauter mean diameter over the flow channel. The meanings of the symbols in Figs. 6 and 8 are found in Table 1. The Sauter mean diameter profile were almost uniform along the channel radius with some increase in size near the wall for the flow conditions where no cap bubbles appeared, namely $\langle j_f \rangle = 0.491$ m/s (●, ▲, ■, ▼), $\langle j_f \rangle = 0.986$ m/s (●, ▲, ■), $\langle j_f \rangle = 2.01$ m/s (●, ▲) and $\langle j_f \rangle = 5.00$ m/s (●, ▲, ■). The relatively larger bubbles near the wall might be due to the highly concentrated bubbles having a greater probability of bubble coalescence. The profiles were not changed significantly as the flow developed, although the bubble size increased up to 10–20% along the flow direction due to the bubble expansion (see Fig. 8). On the other hand, the Sauter mean diameter profile had a core peak for the flow conditions where cap bubbles appeared, namely $\langle j_f \rangle = 0.986$ m/s (▼), $\langle j_f \rangle = 2.01$ m/s (■, ▼) and $\langle j_f \rangle = 5.00$ m/s (■, ▼, ◆, *). As discussed in Section 3.1.1, some of large bubbles formed by the coalescence were transported to the

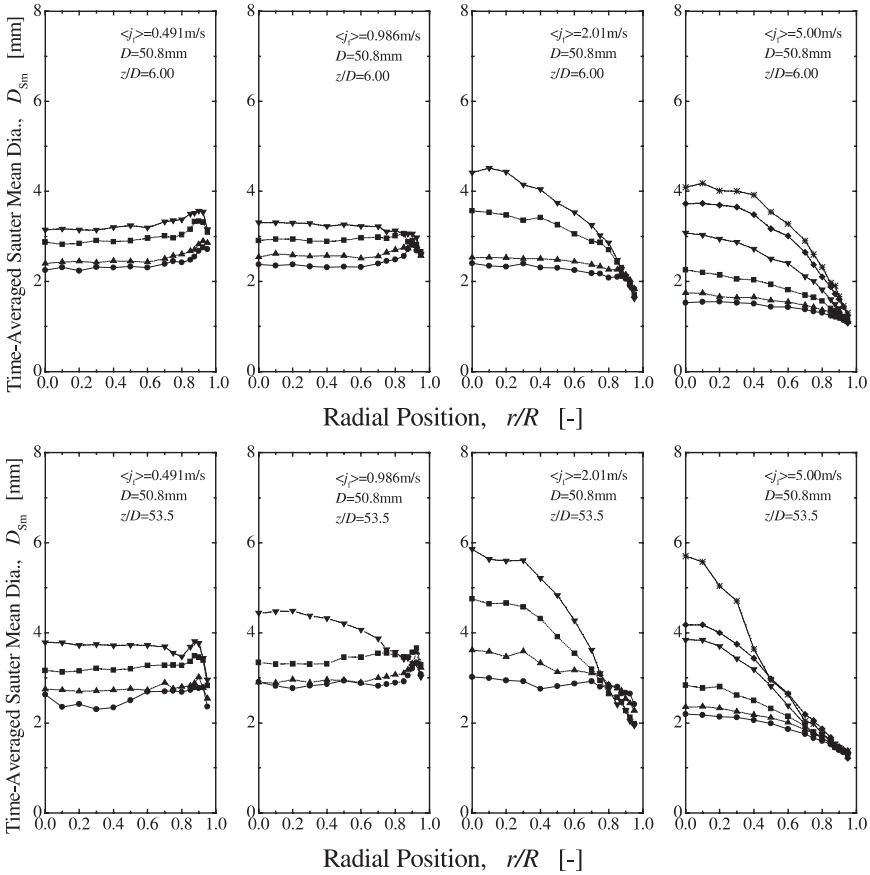

Fig. 8. Local Sauter mean diameter profiles at $z/D = 6.00$ and 53.5.

channel center, since a large bubble (>3.6 mm) tended to migrate toward the channel center [42,44]. The bubble breakup around the channel center might not be marked as compared with the bubble coalescence, because most of turbulence kinetic energy would be produced and dissipated near the wall [46]. On the other hand, the bubble breakup in the vicinity of the wall might be significant due to the strong shear stress, resulting in small bubbles. Consequently, both of the void fraction and bubble size profiles had the core peaks.

3.1.3. Interfacial area concentration

Fig. 9 shows the behavior of interfacial area concentration profiles, corresponding to that of void fraction profiles in Fig. 4. Fig. 6 (upper figures) also shows the axial development of one-dimensional interfacial area concentrations, $\langle a_i \rangle$, obtained by integrating local interfacial area concentration over the flow channel. The meanings of the symbols in Fig. 9 are found in Table 1. As expected for bubbly flow, the interfacial area concentration profiles were similar to the void fraction profiles except for the flow conditions where cap bubbles appeared. Since the interfacial area concentration is directly proportional to the void fraction and the Sauter mean diameter was almost uniform along the channel radius, the interfacial area profiles displayed the same behavior as their respective void fraction profiles. Since the formation of cap bubbles decreased the interfacial area concentration significantly, the interfacial area concentration profiles were different from void fraction profiles. For the flow conditions, the Sauter mean diameter had the core peak, resulting in a flat profile or a concave profile of the interfacial area concentration near the channel center due to the formation of the cap bubbles. For $\langle j_f \rangle = 0.986$ m/s and $\langle \alpha \rangle > 20\%$ (▼), the peak around the channel center in the interfacial area concentration profile was diminished along the flow direction, although the core peaking was observed in the void fraction profile. For $\langle j_f \rangle = 2.01$ m/s and $\langle \alpha \rangle > 15\%$ (■, ▼), the interfacial area concentration profiles became almost flat around the channel center ($r/R < 0.8$), although the core peaking was observed in the void fraction profiles. For $\langle j_f \rangle = 5.00$ m/s and $\langle \alpha \rangle > 15\%$ (■, ▼), concave distributions near the channel center were observed in the interfacial area concentration profiles.

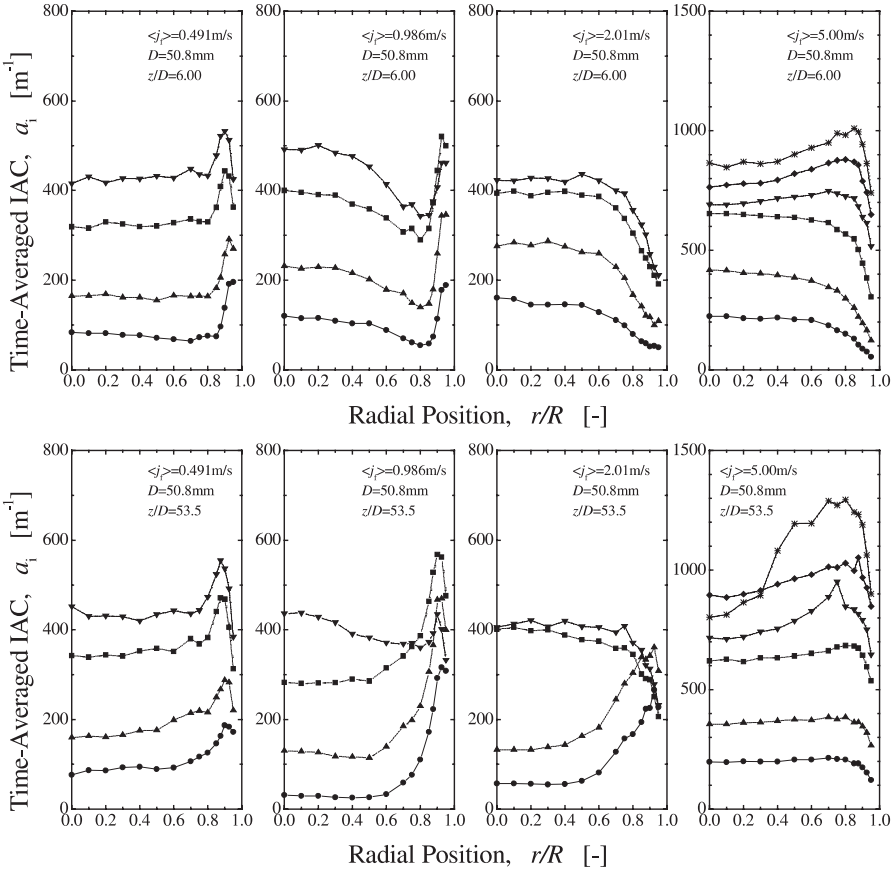

Fig. 9. Local interfacial area concentration profiles at $z/D = 6.00$ and 53.5.

3.1.4. Turbulence intensity

Fig. 10 shows the behavior of turbulence intensity profiles, corresponding to that of void fraction profiles in Fig. 4. The meanings of the symbols in Fig. 10 are found in Table 1. In addition to this, the symbol of open circle means the value measured in a water single-phase flow. Generally, the introduction of bubbles into the liquid flow will cause more agitated flow than in single-phase flow turbulence. As Serizawa and Kataoka [46] pointed out, under certain flow conditions, the two-phase flow turbulence is reduced locally by bubbles, when compared with single-phase flow turbulence intensity for the same liquid flow rate. They explained the enhancement and reduction of two-phase flow turbulence due to the bubble introduction as follows: (1) enhanced energy dissipation and turbulence production in the wall region due to the large gradient of the velocity fluctuation and shear stress distribution there, (2) bubble relative motions which generate additional turbulence, (3) large velocity fluctuation gradient near gas–liquid interfaces increases turbulence energy dissipation, and (4) energy dumping effects of bubbles at interfaces. As shown in Fig. 10, the turbulence intensity reduction phenomena in this experiment was observed locally at $z/D = 53.5$ for three flow conditions such as $\langle j_f \rangle = 0.986$ m/s and $\langle j_{g,0} \rangle = 0.0473$ m/s (●; $\langle \alpha \rangle_{z/D=53.5} = 5.12\%$), $\langle j_f \rangle = 2.01$ m/s and $\langle j_{g,0} \rangle = 0.103$ m/s (●; $\langle \alpha \rangle_{z/D=53.5} = 5.68\%$), and $\langle j_f \rangle = 5.00$ m/s and $\langle j_{g,0} \rangle = 0.245$ m/s (●; $\langle \alpha \rangle_{z/D=53.5} = 5.41\%$). The similar result was also reported by Wang et al. [47] for $\langle j_f \rangle = 0.94$ m/s and $\langle j_g \rangle = 0.10$ m/s ($z/D = 35$, $D = 57.15$ mm). Serizawa and Kataoka [46] suggested that the turbulence reduction occurred roughly at liquid velocities higher than approximately 1 m/s. The present experiment would support the Serizawa–Kataoka's observation. On the other hand, the turbulence intensity enhancement phenomena was observed for $\langle \alpha \rangle > 5\%$ regardless of the liquid velocity.

For the flow conditions where no cap bubbles appeared, the turbulence intensity were almost uniform with some increase near the wall. Michiyoshi and

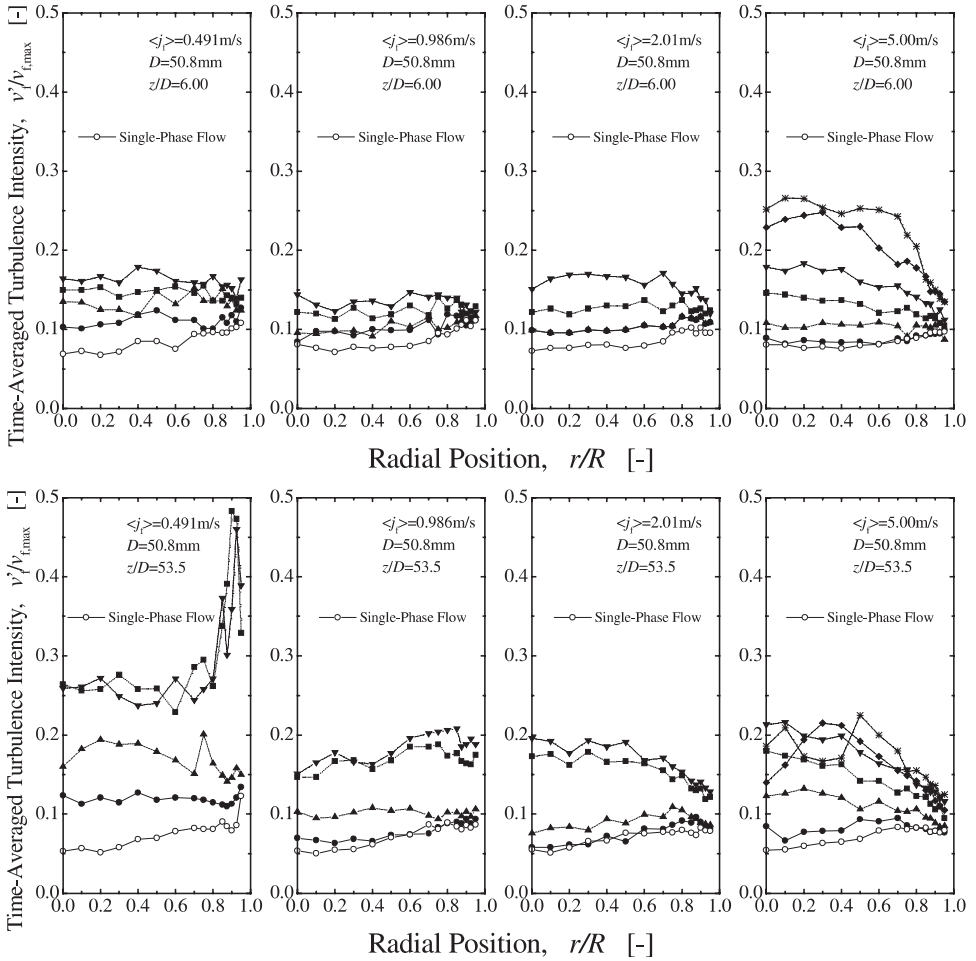

Fig. 10. Local turbulence intensity profiles at $z/D = 6.00$ and 53.5.

Serizawa [48] explained that this peaking in the wall region which was estimated as $D_b/R < r/R < 1$ would reflect agitating bubble motions due to bubble–wall interactions and also the interactions between bubbles and large scale liquid eddies. On the other hand, for the flow conditions where cap bubbles appeared, the turbulence intensity had the core peak. When large bubbles passed through the core, the liquid velocity fluctuation would be significant, resulting in large turbulence intensity.

3.1.5. Interfacial and liquid velocities

Figs. 11 and 12 show the behavior of interfacial and liquid velocities profiles, corresponding to that of void fraction profiles in Fig. 4. The meanings of the symbols in Figs. 11 and 12 are found in Table 1. Dotted lines in the figures indicate the velocity profiles for a fully-developed water single-phase flow. For low liquid velocities ($\langle j_f \rangle \leqslant 1$ m/s), the introduction of bubbles into the liquid flow flattened the liquid velocity profile, with a relatively steep decrease close to the wall as shown in Fig. 12. The liquid velocity profile approached to that of developed single-phase flow with the increase of void fraction. The effect of the bubble on the liquid velocity profile was diminishing with increasing gas and liquid velocities. For high liquid velocities ($\langle j_f \rangle 1$ m/s), the liquid velocity profile came to be the power law profile as the flow developed. The interfacial velocity had the same tendency of the respective liquid velocity profiles as shown in Fig. 11.

3.2. One-dimensional interfacial area transport

In order to develop the one-dimensional interfacial area transport equation, an accurate data set of the area averaged flow parameters is indispensable. One-dimensional interfacial area concentration and Sauter mean diameter are plotted against z/D in Fig. 6. The meanings of the symbols in Fig. 6 are found in Table 1. For $\langle j_f \rangle = 0.491$, 0.986 and 2.01 m/s, and relatively low void fraction, the area averaged Sauter mean diameter as well as the area averaged interfacial area concentration gradually increased along the axial direction, if no cap or relatively large bubbles were formed. Since relatively weak interactions between bubbles, and between bubbles and eddies might be expected in the flow condition, the cause for the increase of the interfacial area con-

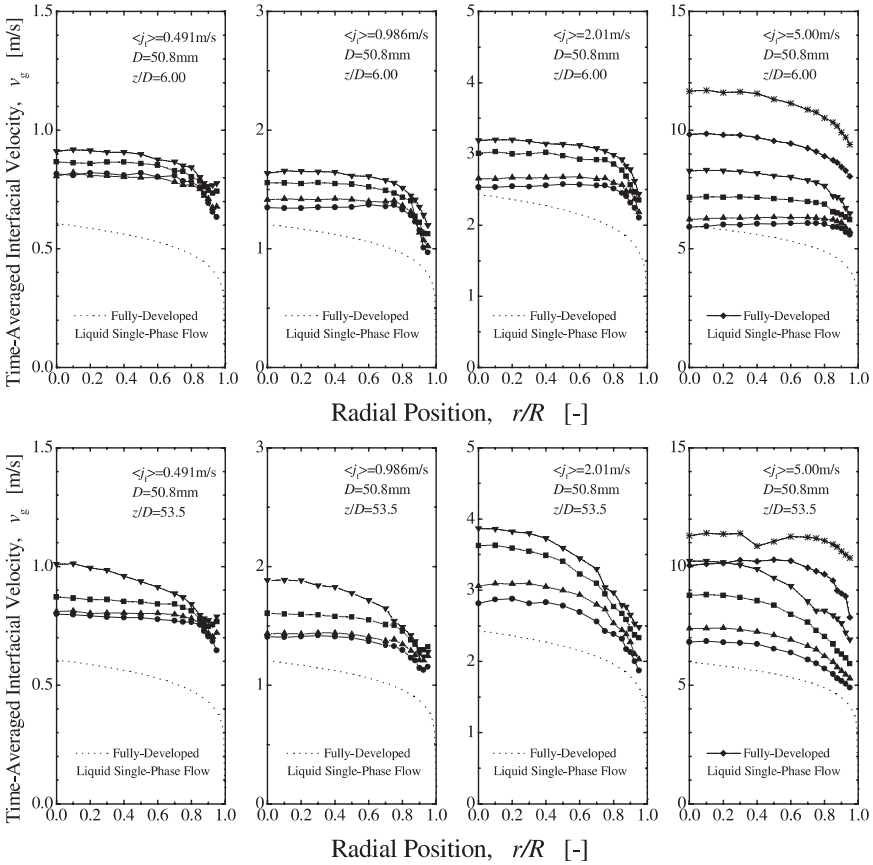

Fig. 11. Local interfacial velocity profiles at $z/D = 6.00$ and 53.5.

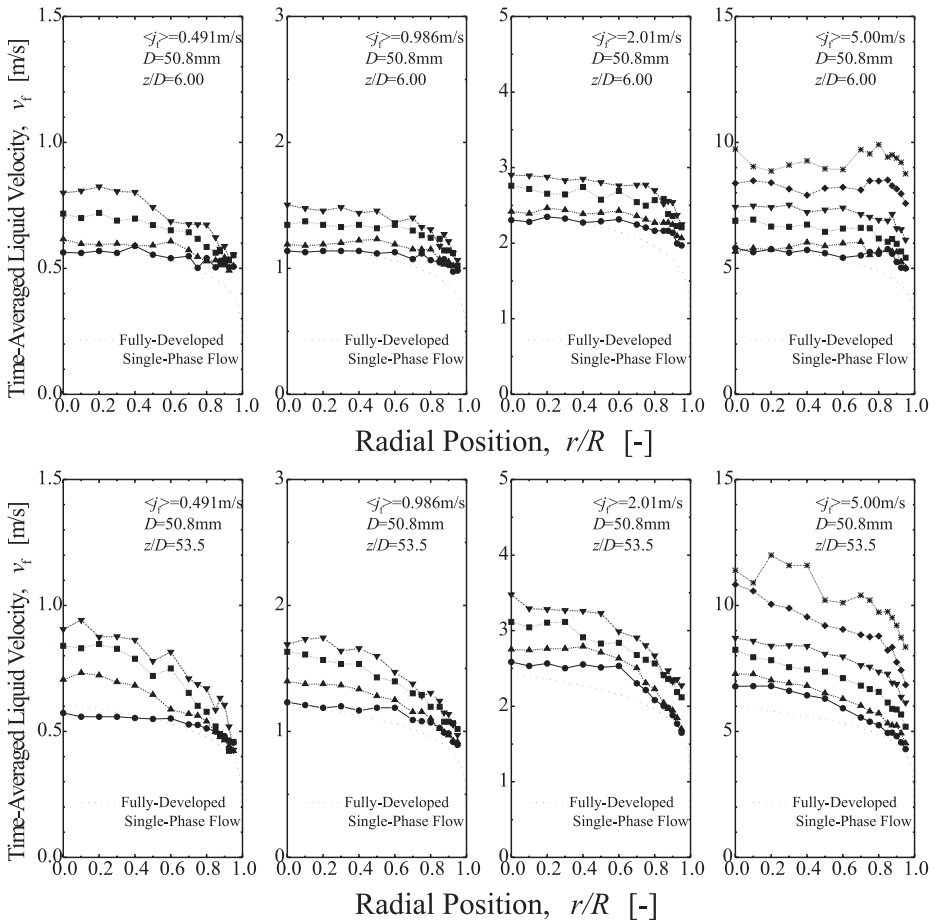

Fig. 12. Local liquid velocity profiles at $z/D = 6.00$ and 53.5.

centration and the Sauter mean diameter might be the gas expansion due to the pressure reduction along the flow direction. For $\langle j_f \rangle = 0.986$ and 2.01 m/s, and relatively high void fraction, the increase rate in the interfacial area concentration was decreased or the decrease in the interfacial area concentration along the axial direction was observed, if cap or relatively large bubbles were formed. For $\langle j_f \rangle = 5.00$ m/s and relatively low void fraction (●, ▲), a strong liquid turbulence might promote the bubble coalescence rather than the bubble breakup, resulting in axial decrease of the interfacial area concentration as well as axial increase in the Sauter mean diameter, whereas for $\langle j_f \rangle = 5.00$ m/s and relatively high void fraction (■, ▼, ◆, *), the dominant mechanism on the interfacial area transport would be likely to change from the bubble coalescence to the bubble breakup, resulting in axial increase in the interfacial area concentration and axial decrease in the Sauter mean diameter.

Since the bubble expansion due to the pressure reduction can be thought of as the source term of the interfacial area transport, the effect of the bubble coalescence and breakup on the interfacial area transport should be extracted to understand the mechanism of the interfacial area transport due to the bubble coalescence and breakup as follows. Ishii et al. [49] derived the one-dimensional and one-group interfacial area transport equation taking the gas expansion along the flow direction into account as

$$\frac{\partial \langle a_i \rangle}{\partial t} + \nabla \cdot \left(\langle a_i \rangle \langle \langle v_g \rangle \rangle_a \right) = \frac{1}{3\psi} \left(\frac{\langle \alpha \rangle}{\langle a_i \rangle} \right)^2 \left[\sum_j \langle S_j \rangle + \langle S_{ph} \rangle \right] + \left(\frac{2\langle a_i \rangle}{3\langle \alpha \rangle} \right) \left[\frac{\partial \langle \alpha \rangle}{\partial t} + \nabla \cdot \left(\langle \alpha \rangle \langle \langle v_g \rangle \rangle \right) \right], \quad (3)$$

where ψ is the factor depending on the shape of a bubble ($1/36\pi$ for a spherical bubble) and S_j, and S_{ph} denote the average local bubble velocity weighted by the bubble number, the source or sink terms in the interfacial area

concentration, respectively. The brackets of $\langle\rangle$, $\langle\langle\rangle\rangle_a$ and $\langle\langle\rangle\rangle$ mean the area averaged quantity, the interfacial area concentration weighted cross-sectional area averaged quantity, and the void fraction weighted cross-sectional area averaged quantity, respectively. Eq. (3) can be simplified as follows on the assumptions of (i) no phase change, (ii) steady flow, and (iii) equilibrium of bubble coalescence and breakup rates.

$$\langle a_{i,eq}\rangle = \left(\frac{P_0}{P}\right)^{2/3}\langle a_{i,0}\rangle, \tag{4}$$

where $a_{i,eq}, a_{i,0}, P$, and P_0 denote the local interfacial area concentration under the conditions of no phase change and equilibrium of bubble coalescence and breakup rates, the inlet interfacial area concentration, the local pressure, and the inlet pressure, respectively. The ratio of area averaged interfacial area concentration, $\langle a_i\rangle$, to $\langle a_{i,eq}\rangle$, $\xi(\equiv \langle a_i\rangle/\langle a_{i,eq}\rangle)$ represents the net change in the interfacial area concentration due to the bubble coalescence and breakup. $\xi > 1$ or $\xi < 1$ implies that the bubble breakup or coalescence is dominant, respectively. It should be noted here that ξ becomes identical to a bubble number density ratio, if further assumptions such as (iv) a spherical bubble and (v) a uniform bubble distribution are made.

$$\frac{\langle a_i\rangle}{\langle a_{i,0}\rangle} = \frac{\langle a_i\rangle}{\langle a_{i,eq}\rangle}\left(\frac{P_0}{P}\right)^{2/3} = \xi\left(\frac{P_0}{P}\right)^{2/3}, \quad \xi \equiv \frac{\langle a_i\rangle}{\langle a_{i,eq}\rangle}. \tag{5}$$

The changes in the interfacial area concentration due to the bubble coalescence and breakup, ξ, are plotted against z/D in Fig. 13. The meanings of the symbols in Fig. 13 are found in Table 1. It should be noted in Fig. 13 that the interfacial area concentration and the pressure at $z/D = 6.00$ were taken as $\langle a_{i,0}\rangle$ and P_0, respectively, and measured P were used in the calculation of ξ. For $\langle j_f\rangle = 0.491$ m/s, the bubble coalescence and breakup seemed to be insignificant for the interfacial area transport, whereas the bubble expansion would be dominant term for the interfacial area transport. For $\langle j_f\rangle = 0.986$ and 2.01 m/s, the bubble coalescence was dominant for the interfacial area transport. For $\langle j_f\rangle = 5.00$ m/s, the dominant mechanism of the interfacial area transport was strongly dependent on the void fraction. The mechanism of the interfacial area transport appeared to change from the bubble coalescence to the bubble breakup at $\langle\alpha\rangle \approx 20\%$.

The interfacial area transport mechanism in a bubbly flow system can be roughly classified into three basic mechanisms, namely bubble coalescence due to the collision between bubbles and the bubble expansion for the sink terms, and the bubble breakup due to the collision between a bubble and a turbulence eddy for the source term [34]. The bubble coalescence would be governed by the collision frequency between bubbles, and the bubble coalescence efficiency. The collision frequency between bubbles would be modeled by taking account of the bubble velocity induced by the liquid turbulence, the void fraction, the bubble diameter, and so on, whereas the bubble coalescence efficiency might be modeled by taking account of the bubble contact time for two bubbles and the time required for coalescence of bubbles. On the other hand, the bubble breakup would be governed by the collision frequency between bubbles and eddies, and the bubble breakup efficiency. The collision frequency between bubbles and eddies would be modeled by taking account of the relative velocity between bubbles and eddies, the void fraction, the eddy

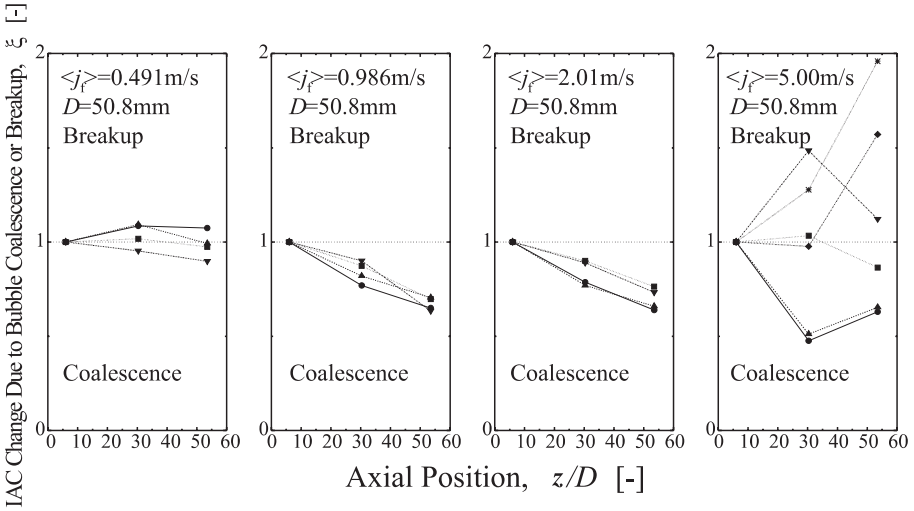

Fig. 13. Interfacial area transport due to bubble coalescence and breakup along flow direction.

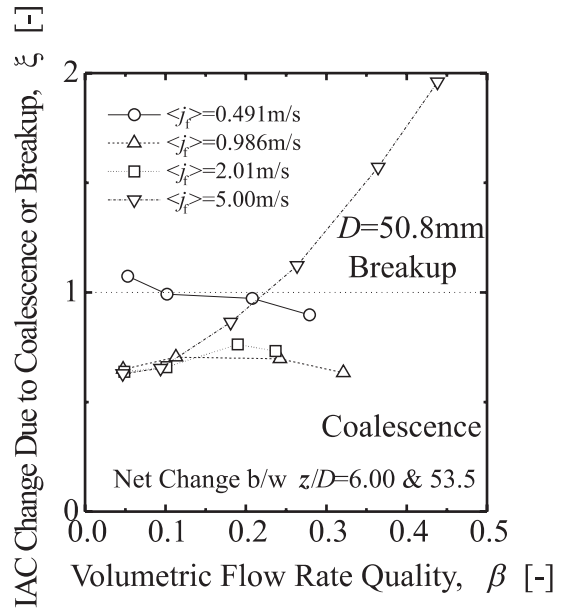

Fig. 14. Dependence of interfacial area transport due to bubble coalescence and breakup on volumetric flow quality.

fraction, the bubble diameter, and so on, whereas the bubble breakup efficiency might be modeled by the eddy energy and the energy required for bubble breakup.

The change in the interfacial area concentration due to the bubble coalescence and breakup between $z/D = 6.00$ and 53.5 are plotted against a volumetric flow rate quality, $\beta(\equiv \langle j_{g,0}\rangle/(\langle j_{g,0}\rangle + \langle j_f\rangle))$ $(\propto\langle\alpha_0\rangle)$, in Fig. 14. For $\langle j_f\rangle = 0.491$ m/s, the weak interactions of bubble-bubble and bubble-eddy due to small liquid turbulence and bubble mixing length would cause $\xi \approx 1$. For $\langle j_f\rangle = 0.986$ and 2.01 m/s, the increase in the liquid velocity would promote the frequency of the collision between bubbles as well as that of between bubbles and eddies but the liquid turbulence might not be large enough to breakup the bubble. Consequently, the bubble coalescence seemed to be dominant for the interfacial area transport. On the other hand, for $\langle j_f\rangle = 5.00$ m/s, the bubble breakup rates were increased with the void fraction, since the increase in void fraction would decrease not only the distance between the bubble and the turbulent eddy, namely the collision frequency between bubbles and eddies, but also the liquid velocity, namely the liquid turbulence.

4. Conclusions

In relation to the development of the interfacial area transport equation, local measurements of the void fraction, interfacial area concentration, interfacial gas velocity, and Sauter mean diameter using the double sensor probe method as well as the liquid velocity and turbulence intensity using hotfilm anemometry were performed extensively for the bubbly flows including the finely dispersed bubbly flow as well as the bubbly-to-slug transition flow at three axial locations of $z/D = 6.00$, 30.3, and 53.5 as well as 15 radial locations. The liquid flow rate and the void fraction ranged from 0.491 to 5.00 m/s and from 5% to 45%, respectively. The mechanisms on the radial profiles of local flow parameters and their axial developments were discussed. The one-dimensional interfacial area transport due to the bubble coalescence and break up was displayed as a function of the volumetric flow quality. For $\langle j_f\rangle = 0.491$ m/s, the rate of the bubble coalescence and break up seemed to be in the equilibrium state. For $\langle j_f\rangle = 0.986$ and 2.01 m/s, the bubble coalescence rate was higher than the bubble break up rate. For $\langle j_f\rangle = 5.00$ m/s, the dominant interfacial area transport phenomena changed from the bubble coalescence to the bubble break up as the void fraction increased. The mechanism of the interfacial area transport was likely to depend on the bubble mixing length, turbulence intensity, void fraction and so on.

The data set obtained in this study are expected to be used for the development of reliable constitutive relations such as the interfacial area transport equation, which reflect the true transfer mechanisms in two-phase flow.

Acknowledgements

The authors would like to acknowledge Dr. Leung (Paul Scherrer Institute, Switzerland), Prof. Wu (Oregon State University, USA), Prof. Bertodano (Purdue University, USA), Dr. Mi (Purdue University, USA), and Dr. Kim (Purdue University, USA) for their valuable discussions. The authors wish to thank Mr. Takada (Kyushu Electric Company, Japan) for his devoted assistance in the data analysis. This work was performed under the auspices of the US Department of Energy's Office of Basic Energy Science. The authors would like to express their sincere appreciation for the encouragement, support and technical comments on this program from Drs. Manley, Goulard, and Price of DOE/BES.

Appendix A

Even in the flow region where cap bubbles appeared, the double sensor probe could be used to measure local measurements of void fraction, interfacial area concentration, and interfacial velocity for small bubbles as well as local measurements of void fraction for cap bubbles. On the other hand, the multi-sensor probe should be used to measure local interfacial area concentration of

cap bubbles instead of the double sensor probe. Although the multi-sensor probe method has been developed [10,13,18,30], a rigorous data base has not been available so far. Since the multi-sensor probe was not available in the present experiment, the one-dimensional interfacial area concentration of cap bubbles was approximately estimated here by the signals from the double sensor probe as follows.

According to Clift et al. [39], the shape of cap bubbles could be closely approximated as a segment of a sphere. For $Re > 150$, the rear or base of the cap bubble was quite flat, though sometimes irregular, and the wake angle of the rising cap bubble in a stagnant fluid was nearly 50°. Recently, it was reported that the wake angle of the rising cap bubble in a forced convective fluid in a round tube was about 90° [50]. Here, the shape of the cap bubble was approximated as a semi-sphere. The cap bubble generally rose faster than a spherical/distorted bubble. However, as the liquid velocity increased, the rise velocity difference between them would come to be negligible. Thus, the rise velocity of the cap bubble was taken to be the same as the total gas velocity. The error due to this assumption would be estimated by the drift flux model [51] to be less than 10% for $\langle j_f \rangle = 2$ m/s,

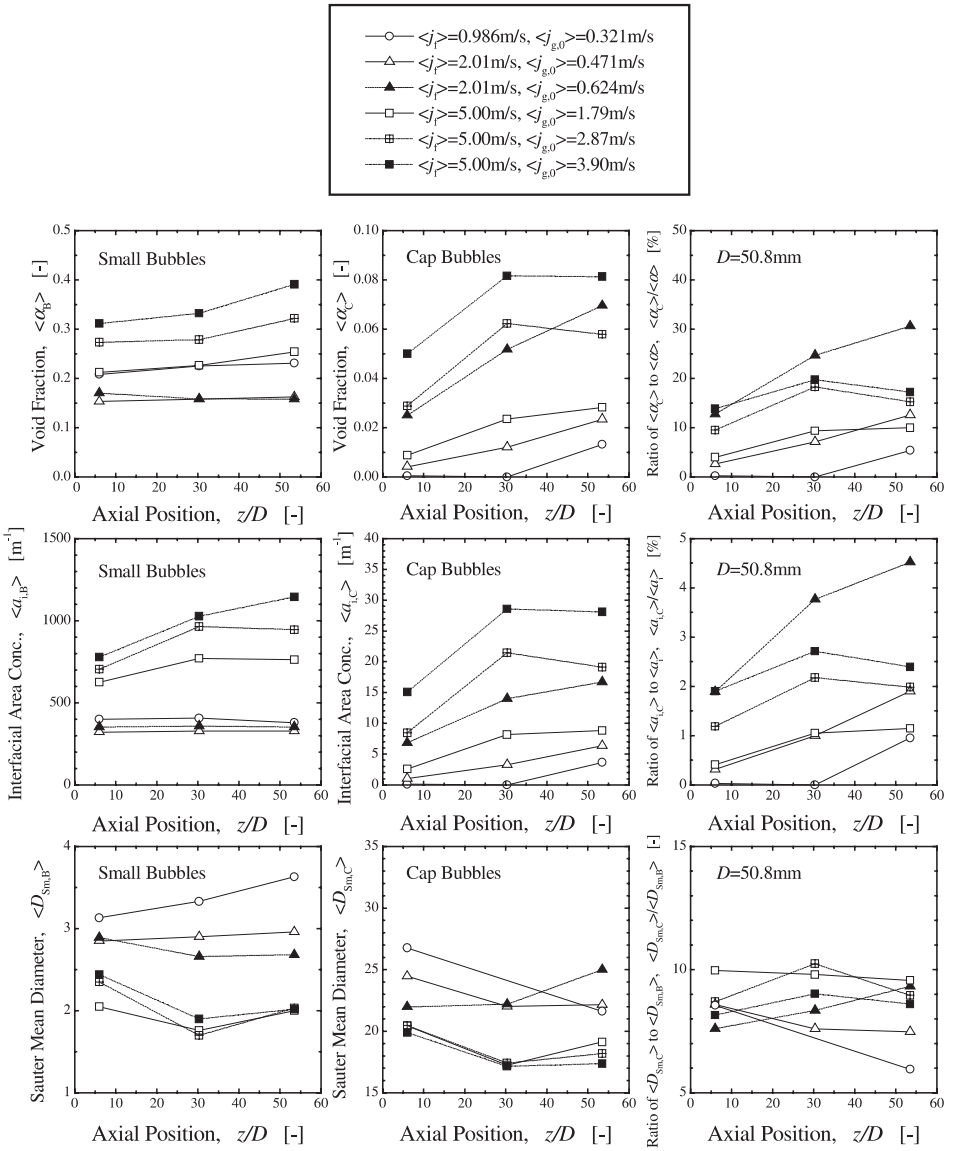

Fig. A1. Axial development of area averaged void fraction, interfacial area concentration and Sauter mean diameter of small bubbles and cap bubbles.

$\langle\alpha\rangle = 0.25$, and $\langle V_{gj,C}\rangle - \langle V_{gj,B}\rangle = 0.30$ m/s by conservative estimates. Here, $\langle V_{gj,C}\rangle$ and $\langle V_{gj,B}\rangle$ mean the drift velocities of cap and small bubbles, respectively. The one-dimensional interfacial area concentration of cap bubbles, $\langle a_{i,C}\rangle$, could be estimated by the following equation with measured superficial gas velocity, $\langle j_g\rangle$, void fraction of cap bubble, $\langle\alpha_C\rangle$, and number of cap bubbles passing the probe per unit time, $N_{b,C}$.

$$\langle a_{i,C}\rangle = 6.24\langle\alpha_C\rangle\left(\frac{N_{b,C}}{\langle j_g\rangle D^2}\right)^{1/3}, \tag{A.1}$$

where D is the tube diameter. Sauter mean diameter, $D_{Sm,k}$ was calculated by the following relation:

$$\langle D_{Sm,k}\rangle = \frac{6\langle\alpha_k\rangle}{\langle a_{i,k}\rangle}. \tag{A.2}$$

Fig. A1 shows the axial change of one-dimensional flow parameters such as void fraction, interfacial area concentration, and Sauter mean diameter of small and cap bubbles. Flow parameters except $\langle a_{i,C}\rangle$ and $\langle D_{Sm,C}\rangle$ were measured directly by the double sensor probe method. Although total void fraction increased along the flow direction due to the pressure reduction, the increase rate in the void fraction of small bubbles, $\langle\alpha_B\rangle$, was diminished by forming cap bubbles. Void fractions of cap bubbles, $\langle\alpha_C\rangle$, were increased monotonically along the axial direction due to the bubble coalescence except for $\langle j_f\rangle = 5.00$ m/s. For $\langle j_f\rangle = 5.00$ m/s, the formation and disintegration of cap bubbles appeared to be in an equilibrium state, resulting in insignificant axial change of $\langle\alpha_C\rangle$ between $z/D = 30.3$ and 53.5. Since the interfacial area concentration was directly proportional to the area-averaged void fraction, the interfacial area changes along the flow direction displayed the same behavior as their respective void fraction changes for constant Sauter mean diameters. It should be noted here that the percentage of $\langle a_{i,C}\rangle$ to $\langle a_i\rangle$ was less than about 3% even for $\langle\alpha_C\rangle/\langle\alpha\rangle \approx 40\%$. This suggested that total interfacial area concentration was mainly attributed to small bubbles in the present flow conditions. Therefore, the estimation error of $\langle a_{i,C}\rangle$ by Eq. (A.1) did not affect the accuracy of $\langle a_i\rangle$ in the flow conditions significantly.

References

[1] M. Ishii, Thermo-fluid dynamic theory of two-phase flow, Collection de la Direction des Etudes et Researches d'Electricite de France, Eyrolles, Paris, France, 22, 1975.

[2] M. Ishii, G. Kojasoy, Interfacial area transport equation and preliminary considerations for closure relations, Technical report, PU-NE-93/6, School of Nuclear Engineering, Purdue University, West Lafayette, IN, USA, 1993.

[3] M. Ishii, Views on the future of thermal hydraulic modeling, in: Proceedings of the OECD/CSNI Workshop on Transient Thermal–Hydraulic and Neutronic Codes Requirements (NUREG/CP-0159), Annapolis, MD, USA, 1996, pp. 751–759.

[4] G. Kocamustafaogullari, M. Ishii, Interfacial area and nucleation site density in boiling systems, Int. J. Heat Mass Transfer 26 (1983) 1377–1387.

[5] J.N. Reyes, Statistically derived conservation equations for fluid particle flows, Trans. Am. Nucl. Soc. 60 (1989) 669–670.

[6] G. Kocamustafaogullari, M. Ishii, Foundation of the interfacial area transport equation and its closure relations, Int. J. Heat Mass Transfer 38 (1995) 481–493.

[7] M. Ishii, Q. Wu, A. Assad, J. Uhle, Interfacial area transport equation for two-fluid model formulation, in: Proceedings of IMuST Meeting, 1998.

[8] C. Morel, N. Goreaud, J.M. Delhaye, The local volumetric interfacial area transport equation: derivation and physical significance, Int. J. Multiphase Flow 25 (1999) 1099–1128.

[9] I. Kataoka, M. Ishii, A. Serizawa, Local formulation and measurements of interfacial area concentration in two-phase flow, Int. J. Multiphase Flow 12 (1986) 505–529.

[10] I. Kataoka, A. Serizawa, Interfacial area concentration in bubbly flow, Nucl. Eng. Des. 120 (1990) 163–180.

[11] G. Kocamustafaogullari, Z. Wang, An experimental study on local interfacial parameters in a horizontal bubbly two-phase flow, Int. J. Multiphase Flow 17 (1991) 553–572.

[12] S.T. Revankar, M. Ishii, Local interfacial area measurement in bubbly flow, Int. J. Heat Mass Transfer 35 (1992) 913–925.

[13] S.T. Revankar, M. Ishii, Theory and measurement of local interfacial area using a four sensor probe in two-phase flow, Int. J. Heat Mass Transfer 36 (1993) 2997–3007.

[14] S. Kalkach-Navarro, R.T. Lahey Jr., D.A. Drew, R. Meyder, Interfacial area density, mean radius and number density measurements in bubbly two-phase flow, Nucl. Eng. Des. 142 (1993) 341–351.

[15] S. Valenti, A. Clausse, D.A. Drew, R.T. Lahey Jr., A contribution to the mathematical modeling of bubbly/slug flow regime transition, Chem. Eng. Commun. 102 (1991) 69–85.

[16] I. Kataoka, M. Ishii, A. Serizawa, Sensitivity analysis of bubble size and probe geometry on the measurements of interfacial area concentration in gas–liquid two-phase flow, Nucl. Eng. Des. 146 (1994) 53–70.

[17] T. Hibiki, S. Hogsett, M. Ishii, Local measurement of interfacial area, interfacial velocity and liquid turbulence in two-phase flow, Nucl. Eng. Des. 184 (1998) 287–304.

[18] S. Kim, X.Y. Fu, X. Wang, M. Ishii, Local interfacial area concentration measurement in a two-phase flow using a four-sensor conductivity probe, Trans. Am. Nucl. Soc. 79 (1998) 356–357.

[19] Q. Wu, M. Ishii, Sensitivity study on double-sensor conductivity probe for the measurement of interfacial area concentration in bubbly flow, Int. J. Multiphase Flow 25 (1999) 155–173.

[20] E. Barrau, N. Riviere, Ch. Poupot, A. Cartellier, Single and double optical probes in air–water two-phase flows: real time signal processing and sensor performance, Int. J. Multiphase Flow 25 (1999) 229–256.

[21] A. Serizawa, I. Kataoka, I. Michiyoshi, Turbulence structure of air–water bubbly flow – I. Measuring techniques, Int. J. Multiphase Flow 2 (1975) 221–233.

[22] T.G. Theofanous, J. Sullivan, Turbulence in two-phase dispersed flows, J. Fluid Mech. 116 (1982) 343–362.
[23] S.K. Wang, S.J. Lee, O.C. Jones Jr., R.T. Lahey Jr., 3D Turbulence structure and phase distribution measurements in bubbly two-phase flows, Int. J. Multiphase Flow 13 (1987) 327–343.
[24] C. Suzanne, K. Ellingsen, R. Risso, V. Roig, Local measurement in turbulent bubbly flows, Nucl. Eng. Des. 184 (1998) 319–327.
[25] A. Serizawa, I. Kataoka, I. Michiyoshi, Phase distribution in bubbly flow, in: Proceedings of the Second International Workshop on Two-Phase Flow Fundamentals, Data Set No.24, 1987.
[26] I. Zun, M. Kljenak, M. Pecar, E. Polutnik, Bubble shape and interfacial area concentration measurements in upward and downward bubbly flow, in: Proceedings of the Second International Conference on Multiphase Flow 1995, Kyoto, Japan, 1995, pp. IN2-9–IN-2-16.
[27] W.H. Leung, S.T. Revankar, Y. Ishii, M. Ishii, Axial development of interfacial area and void concentration profiles measured by double-sensor probe method, Int. J. Heat Mass Transfer 38 (1995) 445–453.
[28] T.J. Liu, The role of bubble size on local interfacial characteristics in two-phase bubbly flow, Nucl. Sci. J. 32 (1995) 120–133.
[29] C. Grossetete, Experimental investigation and preliminary numerical simulations of void profile development in a vertical cylindrical pipe, in: Proceedings of the Second International Conference on Multiphase Flow 1995, Kyoto, Japan, 1995, pp. IF1-1–IF10-10.
[30] W.H. Leung, C.S. Eberle, Q. Wu, T. Ueno, M. Ishii, Quantitative characterizations of phasic structure developments by local measurement methods in two-phase flow, in: Proceedings of the Second International Conference on Multiphase Flow 1995, Kyoto, Japan, 1995, pp. IN2-17–IN2-25.
[31] S. Hogsett, M. Ishii, Local two-phase flow measurements using sensor techniques, Nucl. Eng. Des. 175 (1997) 15–24.
[32] T. Hibiki, M. Ishii, Experimental study on interfacial area transport in bubbly two-phase flows, Int. J. Heat Mass Transfer 42 (1999) 3019–3035.
[33] Q. Wu, S. Kim, M. Ishii, S.G. Beus, One-group interfacial area transport in vertical bubbly flow, Int. J. Heat Mass Transfer 41 (1998) 1103–1112.
[34] T. Hibiki, M. Ishii, One-group interfacial area transport of bubbly flows in vertical round tubes, Int. J. Heat Mass Transfer 43 (2000) 2711–2726.
[35] T. Hibiki, M. Ishii, Two-group interfacial area transport equations at bubbly-to-slug flow transition in a vertical round pipe, in: Proceedings of 34th National Heat Transfer Conference, Pittsburgh, PA, USA, 2000. To be also published in Nucl. Eng. Des.
[36] H. Städtke, A. Blahak, B. Worth, Modeling of transport of interfacial area concentration in two-phase flow systems, in: Proceedings of Eighth International Topical Meeting on Nuclear Reactor Thermal-Hydraulics, Kyoto, Japan, 1997, pp. 69–78.
[37] T. Hibiki, W.H. Leung, M. Ishii, Measurement method of local interfacial area in two-phase flow using a double sensor probe, Technical report, PU-NE-97/5, School of Nuclear Engineering, Purdue University, West Lafayette, IN, USA, 1997.
[38] W. Hilgert, H. Hofmann, Characterization of gas phase flow in bubble columns at low superficial gas velocities with the aid of ultrasonic Doppler techniques, Germany Chem. Eng. 9 (1986) 180–190.
[39] R. Clift, J.R. Grace, M.E. Weber, Bubbles Drops and Particles, Academic Press, New York, 1978.
[40] T. Hibiki, W.H. Leung, M. Ishii, Measurement method of local turbulence in two-phase flow using hotfilm anemometry, Technical report, PU-NE-97/6, School of Nuclear Engineering, Purdue University, West Lafayette, IN, USA, 1997.
[41] T.J. Liu, Bubble size and entrance length effects on void development in a vertical channel, Int. J. Multiphase Flow 19 (1993) 99–113.
[42] A. Serizawa, I. Kataoka, Phase distribution in two-phase flow, in: N.H. Afgan (Ed.), Transient Phenomena in Multiphase Flow, Hemisphere, Washington DC, 1988, pp. 179–224.
[43] Y. Taitel, D. Bornea, E.A. Dukler, Modelling flow pattern transitions for steady upward gas–liquid flow in vertical tubes, AIChE J. 26 (1980) 345–354.
[44] I. Zun, Transition from wall void peaking to core void peaking in turbulent bubbly flow, in: N.H. Afgan (Ed.), Transient Phenomena in Multiphase Flow, Hemisphere, Washington DC, 1988, pp. 225–245.
[45] T. Otake, S. Tone, K. Nakao, Y. Mitsuhashi, Coalescence and breakup of bubbles in liquids, Chem. Eng. Sci. 32 (1977) 377–383.
[46] A. Serizawa, I. Kataoka, Turbulence suppression in bubbly two-phase flow, Nucl. Eng. Des. 122 (1990) 1–16.
[47] S. Wang, S. Lee, O.C. Jones Jr., R.T. Lahey Jr., 3-D turbulence structure and phase distribution measurements in bubbly two-phase flows, Int. J. Multiphase Flow 13 (1987) 327–343.
[48] I. Michiyoshi, A. Serizawa, Turbulence in two-phase bubbly flow, Nucl. Eng. Des. 95 (1986) 253–257.
[49] M. Ishii, Q. Wu, S.T. Revankar, T. Hibiki, W.H. Leung, S. Hogsett, A. Kashyap, Interfacial area transport in bubbly flow, in: Proceedings of 15th Symposium on Energy Engineering Science, Argonne, IL, USA, 1997.
[50] G. Morita, Y. Nakahara, Y. Makino, A. Tomiyama, Study on terminal rising velocity and shape of single bubbles moving in a vertical pipe, in: Proceedings of 18th Multiphase Flow Symposium 1999, 1999, p. 7.
[51] M. Ishii, One-dimensional drift-flux model and constitutive equations for relative motion between phases in various two-phase flow regimes, Technical report, ANL-77-47, Argonne National Laboratory, Argonne, IL, USA, 1977.